Site-specific halloysite functionalization by polydopamine: a new synthetic route for potential near infrared-activated delivery system

Maria Laura Alfieri,[†a] Marina Massaro,[†b] Marco d'Ischia,[*a] Gerardino D'Errico,[a] Noemi Gallucci,[a] Michelangelo Gruttadauria,[b] Mariano Licciardi,[c] Leonarda F. Liotta,[d] Giuseppe Nicotra,[e] Gianfranco Sfuncia,[e] and Serena Riela[*b]

[a] Dipartimento di Scienze Chimiche, Università di Napoli Federico II, Via Cinthia 4, I-80126 Napoli, Italy. E-mail: marco.dischia@unina.it

[b] Dipartimento Scienze e Tecnologie Biologiche Chimiche e Farmaceutiche (STEBICEF), Sez. Chimica, Università degli Studi di Palermo, Viale delle Scienze, Ed. 17, 90128 Palermo, Italy. E-mail: serena.riela@unipa.it.

[c] Dipartimento di Scienze e Tecnologie Biologiche Chimiche e Farmaceutiche (STEBICEF), sez. Chimica e Tecnologie Farmaceutiche, Università degli Studi di Palermo, Via Archirafi, 32, 90123, Italy.

[d] Istituto per lo Studio dei Materiali Nanostrutturati (ISMN)-CNR, Via Ugo La Malfa 153, 90146 Palermo, Italy.

[e] CNR-IMM, Zona Industriale Strada VIII, 5, 95121 Catania, Italy.

[†] Contributed equally

The manuscript is dedicated to the memory of Prof. Sergio Rosselli.

ABSTRACT. Halloysite nanotubes (HNTs) represent a versatile core structure for the design of functional nanosystems of biomedical interest. However, the development of selective methodologies for the site-controlled functionalization of the nanotubes at specific sites is not an

29 easy task. This study aims to accomplish a procedure for the site-selective/specific, "pin-point",

30 functionalization of HNTs with polydopamine (HNTs@PDA). This goal was achieved, at pH

31 6.5, by exploiting the basicity of ZnO nanoparticles anchored on the HNTs external surface

32 (HNTs@ZnO) to induce a punctual polydopamine polymerization and coating. The morphology

33 and the chemical composition of the nanomaterial was demonstrated by several techniques.

34 Turbidimetric analysis showed that PDA coating affected the aqueous stability of HNTs@PDA

35 compared to both HNTs@ZnO and HNTs. Notably, hyperthermia studies revealed that the

36 nanomaterial induced a local thermic rise, up to 50 °C, under near-infrared (NIR) irradiation.

37 Furthermore, secondary functionalization of HNTs@PDA by selective grafting of biotin onto the

38 PDA coating followed by avidin binding was also accomplished.

39 **INTRODUCTION.** Functionalization of nanomaterials is of critical relevance to a variety

40 of biomedical applications, mainly including drug delivery in *e.g.,* cancer therapy. The

41 availability of versatile strategies to tailor and control the physical and chemical

42 properties of nanomaterials and the nature of the functionalities introduced onto them is

43 critical for obtaining highly multifunctional nanomaterials with additional properties

44 compared to the pristine ones.[1]

45 In this framework, halloysite nanotubes (HNTs), an aluminosilicate clay

46 $(Al_2Si_2O_5(OH)_4 \cdot nH_2O)$ with a predominantly tubular structure, have attracted

47 considerable attention for their ability to entrap, protect and provide sustained release of

48 drugs.[2] In fact, halloysite has a positively charged lumen, mostly consisting of

49 aluminum hydroxide, whereas the external surface, is negatively charged, consisting of

50 silicon dioxide. Generally, HNTs have a length in the range of 0.2–1.5 µm, with inner and

51 outer diameters in the ranges of 10–30 nm and 40–70 nm, respectively. Owing to the high

52 mechanical strength and good biocompatibility, HNTs represent a versatile core structure

53 for the design of functional nanosystems of potential technological and biomedical

54 interest,[2, 3] including *e.g.* catalytic supports,[4-7] adsorbent nanomaterials[8, 9] and

55 nanofillers.[10] Furthermore, due to the presence of an empty lumen they can be

56 effectively used as nanocontainers for drugs, making them more attractive than other

57 nanomaterials such as biodegradable porous nanosilica. In most cases, design of

58 functional system relies on selective functionalization of the nanotubes at specific sites,

59 such as at the inner and/or the outer surface,[10-12] or on substructural patterning, which

60 is not an easy task.

61 To this aim, interesting perspectives toward a rational and controlled manipulation of the

62 nanomaterials have been opened by the reliance on the substrate-independent underwater

63 adhesion properties of mussel-inspired polydopamine (PDA) which allow to achieve

64 HNTs functionalization and to provide an effective means of secondary functionalization.

65 In addition, PDA possesses an intrinsic biocompatibility and a good absorption towards

66 near-infrared light (NIR) around 808 nm, which makes it capable of converting photons

67 into thermal energy adding further properties to the resulting nanomaterials.[13-16]

68 A systematic investigation of the interaction between halloysite surfaces and dopamine

69 as a function of pH[17] revealed a strong influence of the surface and reaction conditions

70 on the chemical properties of the PDA coating. Key observations included: a) a different

71 thickness of the coating layers on the external surface of halloysite (*ca.* 5 nm) *versus* the

72 inner surface (thinner), which was attributed to the small dimension of the lumen (~15

73 nm); b) the occurrence of different structural and chemical properties of PDA coatings on

74 halloysite *vs* free PDA, as apparent from the lower proportion of carbonyl and cyclized

75 amine groups in the former case, which reflects a decreased tendency to oxidation of the

76 halloysite-bound catechol groups; c) a prominent proportion of primary amine groups at

77 acidic pH.[18]

78 The coating of halloysite with PDA[17, 19-23] or the covalent functionalization of the

79 alumina inner lumen with dopamine molecules was investigated in a number of

80 studies.[24] Nanocomposites produced by functionalization of the external surface of

81 HNTs with PDA were used for example to provide enhanced anti-fouling, bio-fouling and

82 filtration properties to polyetherimide (PEI) membranes.[25]

83 We, recently, reported the preparation of PDA/HNTs nanocomposites, synthesized

84 under both acidic and alkaline oxidation conditions.[26] HNTs, used as fillers, were found

85 to interact in different ways with PDA depending on the pH of the medium, producing

86 various effects on nanocomposite morphology, including an increase in the thermal

87 stability of PDA samples based on thermogravimetric analysis (TGA). The PDA/HNTs

88 nanocomposites imparted morphologies to a glass surface similar to those of the bulk

89 polymers and, affected transparency and wettability by enhancing surface roughness.

90 Although functionalization of HNTs has emerged as a very promising strategy to
91 modify and tailor PDA-based surface functionalization, available protocols for PDA
92 deposition on HNTs require alkaline conditions[27] or the use of oxidants, causing
93 extensive precipitation of polymer in the reaction medium. The development of selective
94 methodologies for the site-controlled functionalization of HNTs appears therefore to be
95 an important goal for various technological and biomedical applications.

96 Herein we report, the first procedure, to the best of our knowledge, for the site-
97 selective/specific, "pin-point", nanofunctionalization of HNTs with PDA (HNTs@PDA),
98 which exploits the basicity of ZnO nanoparticles decorating the external surface of HNTs
99 (HNTs@ZnO) to induce surface-specific polymerization and deposition of dopamine
100 coatings at relatively low pH (6.5) under conditions hindering polymer precipitation in the
101 bulk mixture. Hyperthermia studies revealed that HNTs@PDA can induce a local thermic
102 rise under NIR irradiation with good photothermal stability for at least four consecutive
103 cycles of laser on/off operations. Furthermore, the nanomaterial displayed good properties
104 as an anchoring point for the grafting of biotin and subsequent avidin interaction, to
105 obtain a potential drug delivery system with therapeutic synergies. These results open the
106 doorway to novel strategies for mussel-inspired nanofunctionalization and nanopatterning
107 for development of multifunctional delivery systems.

108 **MATERIALS AND METHODS.** Dopamine hydrochloride ($\leq$ 100%), HNTs (nanopowder,
109 MQ100), ZnO (nanopowder, 81%) and HABA/Avidin reagent (lyophilized powder, MQ200)
110 were purchased from Merck (Darmstadt, Germany) and used without further purification.
111 HNTs@ZnO nanomaterial and biotin 2'-aminoethylamide (**1**) were synthetized as reported in
112 literature.[28, 29]

113 UV–*vis* measurements were performed using a Beckmann DU 650 spectrometer.

114 The morphologies of the nanocomposites were studied using an ESEM FEI QUANTA 200F
115 microscope. Before each experiment, the surface of the sample was coated with gold in argon by
116 means of an Edwards Sputter Coater S150A to avoid charging under electron beam treatment.
117 The energy of the beam was 20 keV, and the working distance was 10 mm. Minimal electron
118 dose conditions were employed to avoid damaging the sample.

119   Fourier Transform-Infrared Spectroscopy (FT-IR) analyses were recorded with an Agilent
120   Technologies Cary 630 FT-IR spectrometer. Specimens for these measurements were prepared
121   by mixing 5 mg of the sample powder with 100 mg of KBr.

122   The thermogravimetric analysis (TGA) of the material was performed in a TGA/DSC1 STAR
123   System from Mettler Toledo Inc. The sample (15 mg) was subjected to a pre-treatment in air
124   flow (30 mL/min) from 25 °C to 100 °C with a heating rate of 10 °C/min and holding time at 100
125   °C for 30 min, to remove any eventual physisorbed water. Then, the temperature was increased
126   from 100 to 1000 °C under air flow (30 mL/min) and the weight loss occurring during this step
127   was considered to calculate the organic weight content of the HNTs@ZnO nanomaterial.

128   The Transmission Electron Microscopy acquired in Scanning mode (STEM) were performed
129   with a FEI TECNAI F20 microscope operating at 200 keV. The instrument is also equipped with
130   a dispersion micro-analysis of energy (EDS) and the STEM accessory. STEM pictures were
131   recorded using a High Angle Annular Dark Field (HAADF) detector: in this imaging mode, the
132   intensity I is proportional to $Z^{1.7}t$, where Z is the mean atomic number and t is the thickness of
133   the specimen. The powder was dispersed in isopropyl alcohol and sonicated for 10 min. The
134   solution was then drop casted on an ultrathin carbon film supported by a gold grid. The
135   preparation was then dried at 50 °C.

136   Attenuated Total Reflectance-Fourier Transform Infrared Spectroscopy (ATR-FTIR) spectra
137   have been acquired by using an FT-IR Bruker Lumos equipped with Platinum ATR. Spectra
138   result from 60 scans in the wavenumber range 1400–400 cm^{-1}, with resolution of 2 cm^{-1}. The
139   baseline correction has been performed by using the OPUS® software.

140   The size analysis, ζ-potential and polydispersity index of the samples were determined using a
141   Malvern Zetasizer Nano ZS instrument, fitted with a 532-nm laser at a fixed scattering angle of
142   173°.

143   High Performance Liquid Chromatography (HPLC) analyses were performed on an Agilent
144   1100 binary pump instrument equipped with an SPD-10AV VP UV-visible detector using a
145   Synergi Hydro-RP80A column, 250 mm x 4.6 mm, 4 μm particle size at 0.7 mL/min. Detection
146   wavelength was set at 254 and 280 nm. Eluant system: 1% formic acid taken to pH = 2.8 with
147   sodium hydroxide/methanol 97:3 (v/v).

148   Electron Paramagnetic Resonance (EPR) measurements were performed using an X-band (9
149   GHz) Bruker Elexys E-500 spectrometer (Bruker, Rheinstetten, Germany), equipped with a

superhigh sensitivity probe head. Samples (4.9−7.6 mg) were transferred to flame-sealed glass capillaries which were coaxially inserted in a standard 4 mm quartz sample tube, accurately positioned inside the cavity. Measurements were performed at room temperature. The instrumental settings were as follows: sweep width, 140 G; resolution, 1024 points; modulation frequency, 100 kHz; modulation amplitude, 1.0 G. The amplitude of the field modulation was preventively checked to be low enough to avoid detectable signal overmodulation. EPR spectra were measured with a microwave power of ~0.25 mW to avoid microwave saturation of resonance absorption curve. A total of 128 scans were accumulated to improve the signal-to-noise ratio. For power saturation experiments, the microwave power was gradually incremented from 0.008 to 127 mW. The g value and the spin density were evaluated by means of an internal standard, Mn^{2+}-doped MgO, prepared as previously described.[30]

2.1 Synthesis of HNTs@PDA nanomaterial

HNTs@PDA nanomaterial was prepared by adding 0.4 g of HNTs@ZnO nanomaterial to a 20 mL of dopamine hydrochloride solution (1.6 mM) in phosphate buffer (50 mM) at pH 6.5, under inert atmosphere by bubbling Ar into the solution. The mixture was stirred for 10 h or 24 h at room temperature. Afterwards, the dispersion was centrifuged, and the solid precipitate was washed several times with deionized water (*ca.* 200 mL). The grey powder obtained was dried at 60 °C overnight.

2.2 Chemical degradation of HNTs@PDA nanomaterial

The appropriate sample (150 mg of HNTs@PDA and HNTs@ZnO or 5 mg of polydopamine samples) was suspended in 1 M NaOH (1 mL) and treated with 1.5% H_2O_2 at room temperature and under vigorous stirring. After 18 h, the mixture was acidified to pH = 2 with 0.2 M HCl, filtered through nylon membranes (0.45 µm) and analyzed by HPLC.[31]

2.3 Evaluation of the hyperthermic effect of HNTs@PDA

A dispersion of HNTs@PDA in water (20 mL, 10 mg mL^{-1} which correspond to PDA amount in the nanomaterial of 160 mg mL^{-1}) was prepared and treated with an 810 nm diode laser (GBox 15A/B by GIGA Laser) with the power fitted at either 0.5 or 0.7 W cm^{-3} as reported elsewhere. [32, 33] At fixed intervals, the temperature of the dispersion was recorded and reported as a function of the exposure time. The same experiment was carried out on pristine HNTs and HNTs@ZnO as control.

The 810 nm diode laser used for this study was chosen as it is normally recognized as safe for

humans and used in various fields of clinical therapy. [34]

2.4 Biotinylation of HNTs@PDA nanomaterial

In a 10 mL round bottom flask were introduced 35 mg of HNTs@PDA and 5 mL of EtOH. Afterwards, 40 mg (0.14 mmol) of biotin 2'-aminoethylamide (**1**) were added and the dispersion was left to stir at reflux for 18 h. Then the solid was washed several times with water and dried at 60 °C overnight.

2.5 Interaction with HABA/Avidin and determination of biotin grafted onto HNTs@PDA nanomaterial

To a 900 μL of a stock solution of HABA/Avidin reagent in deionized water, 100 μL of a biotinylated HNTs@PDA dispersion (0.6 or 6 mg mL^{-1}) were added and the change in absorption intensity of HABA (λ_{max} = 500 nm) was monitored.

2.6 Statistical analysis

In all the experiments, each sample was tested in independent analyses, each carried out in triplicate. The results are presented as the mean ± standard deviation (SD) values obtained.

RESULTS AND DISCUSSION. The HNTs@ZnO nanomaterial was synthesized by a reported procedure.[28] In brief, to a suspension of ZnO nanoparticles in phosphate buffer solution (pH= 8.0), pristine HNTs were added, to obtain HNTs@ZnO as a suspension, following the formation of covalent bonds between Zn^{2+} ions and HNTs outer surface.

Selective coating of ZnO nanoparticles onto HNTs@ZnO to give HNTs@PDA was accomplished by addition of HNTs@ZnO to 20 mL of dopamine hydrochloride solution (1.6 mM) in 50 mM phosphate buffer at pH 6.5 for 10 or 24 h (Scheme 1). Under these conditions, PDA deposition was immediately apparent from the fast color change from whitish to pale grey, whereas no color change was apparent with pristine HNTs in a control experiment. Under these conditions the dopamine solution was stable without visible polymerization and PDA precipitation even after 24 h.
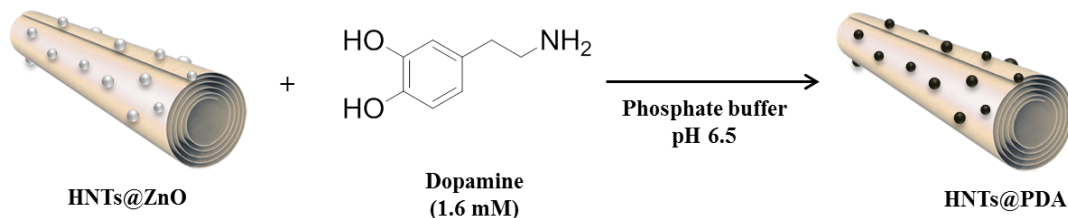
Dynamic light scattering (DLS) measurements gave clear indications of dopamine polymerization onto the HNTs@ZnO in phosphate buffer at pH 6.5. By this technique, indeed, it was possible to calculate the average translational diffusion coefficient (Figure S1) which is related to the dimension and shape of the diffusing particles, their hydration, solvent viscosity, and aggregation phenomena. HNTs are anisotropic objects with a high aspect ratio, which can change due to functionalization. Moreover, particles ability to interact and aggregate can also depend on surface decoration. Thus, a detailed quantitative analysis of the results was hampered. Valuable information was achieved by using the Stokes-Einstein equation to calculate the average diameter of the equivalent sphere, which can be considered as an index to follow the changes in particle dimensions and interparticle aggregation.

Figure 1 shows that in the early stages of the process the average diameter was similar to that of HNTs@ZnO nanomaterial (Table 1), and then gradually increased. It is interesting to note that the Z-average sizes (*i.e.*, the intensity weighted mean diameters) of pristine HNTs and HNTs@ZnO nanomaterials remain unaltered during time. Thus, the size increase is caused by the PDA formation onto the HNTs@ZnO nanomaterial. After 10 h the HNTs@PDA nanoparticles size was apparently very large (> 1000 nm) with a high polydispersity index (PI) as large as *ca.* 0.56. It is worth mentioning here that PI is a dimensionless number calculated from a simple two-parameter-based cumulant analysis of DLS data and it is a measure of the heterogeneity of a sample based on size. Values smaller than 0.05 are, indeed, attributed to monodisperse particle.[35] In our case, the results indicated a broad size distribution of diffusing objects. Noticeable, the Z-average size of HNTs@ZnO proved to be slightly larger than that of HNTs (Table 1), probably suggesting agglomeration in the aqueous medium. The significant increase in the average diameter following PDA coating was attributed to favorable supramolecular interactions

234 mediated by the PDA-coated sites on the HNTs external surface and, therefore, to a
235 collective motion of nanoparticles.[36]
236 The effect of the PDA coating on the surface charge of HNTs was investigated by
237 ζ–potential measurements in 50 mM phosphate buffer at pH 6.5 (Table 1). Whilst
238 HNTs@ZnO displayed a surface charge similar to that of pristine HNTs, following PDA
239 coating the surface charge became slightly more positive suggesting protonated amine
240 groups in the HNTs@PDA structure at pH 6.5.

241
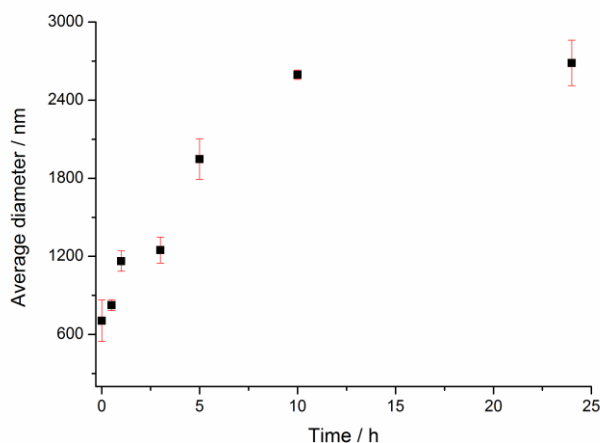
Figure 1. Trend of the average diameter of the HNTs@PDA nanomaterial with time in phosphate buffer (50 mM) at pH 6.5. Reported are the mean ± SD values of three independent experiments run in triplicate.

Table 1. Average diameter, polydispersivity index and ζ–potential values for HNTs, HNTs@ZnO and HNTs@PDA nanomaterials. Reported are the mean ± SD values of three independent experiments run in triplicate.

Sample	Z-average size (nm)	PI	ζ-potential (mV)
HNTs	570 ± 70	0.60	-34 ± 4
HNTs@ZnO	750 ± 160	0.36	-38 ± 8
HNTs@PDA	1320 ± 110	0.57	-26 ± 6

249
250 Scanning Electron Microscopy (SEM) images showed that HNTs@PDA (Figure 2b-c), in
251 contrast with the HNTs@ZnO precursor (Figure 2a) and pristine HNTs (Figure S2), displays a
252 compact structure keeping HNTs sticked together; however, the tubular shape of HNTs is still
253 observable. The observed morphology could be reasonably ascribed to π–π interactions caused
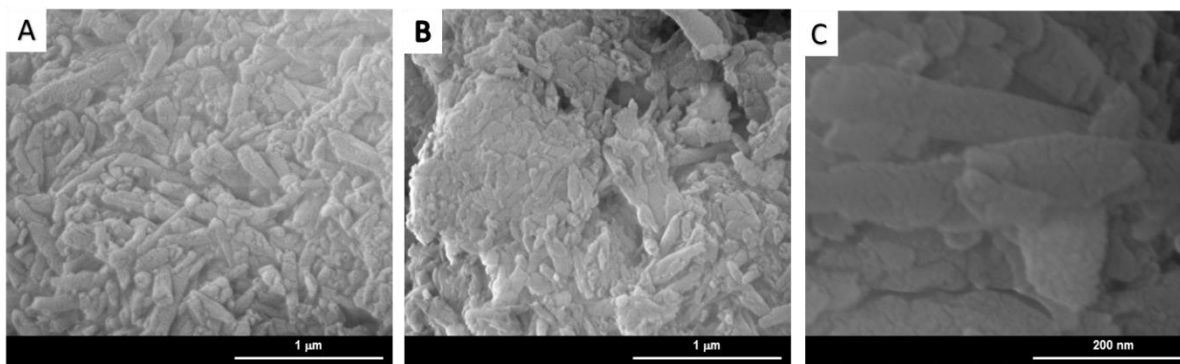254 by the PDA coated nanoparticles onto the HNTs external surface.[37]

9

**Figure 2.** SEM images of (a) HNTs@ZnO and (b-c) HNTs@PDA.

High Angle Annular Dark Field Scanning TEM (HAADF-STEM) imaging showed that the tubular structure of HNTs (Figure 3a) with an empty lumen was not significantly affected in HNTs@PDA. The ZnO nanoparticles were clearly visible because of their brighter intensity due to their higher atomic number and proved to be uniformly distributed on the HNTs support (Figure 3a-b).

STEM Spectrum Imaging (SI) mode allowed to collect Energy Dispersive X-ray Spectroscopy (EDS) and Electron Energy Loss Spectroscopy (EELS) at each pixel position over a nanoparticle-containing region (yellow square in Figure 3b). The EDS spectrum was obtained by integration over the entire region and confirmed the presence of C and N atoms from the PDA coating onto HNTs@PDA nanomaterial besides the Zn, Al, Si and O atoms related to the inorganic support. Noteworthy, the EDS analysis performed on different regions of HNTs, where ZnO is not anchored, highlighted the absence of C and N elements, indicating a selectivity in the coating which occurred on a specific site (the basic ZnO) and not on the overall HNTs surface, in agreement with the experimental procedure adopted for the synthesis of HNTs@PDA.

Furthermore, the pin-point functionalization was also confirmed by STEM SI EDX/EELS bidimensional elemental mapping results (Figure 3c). EELS spectroscopy is more sensitive with light element like C, and more localized than EDS techniques. Conversely, the latter one is most effective for the detection of heavier elements like Zn. Statistical analysis indicated the presence of small nanoparticles on HNTs@PDA with an average diameter of 3.3 ± 0.5 nm and narrow size distribution (Figure 3d). Compared to the ZnO nanoparticles onto HNTs@ZnO (*ca.* 2.4 nm) (see Figure S3), we observed an increase in the average nanoparticle dimension caused by a coating as thick as of *ca.* 1 nm. However,

10

the thickness of the applied coating on the ZnO nanoparticles can hardly be estimated from TEM measurements. Based on the nature of the material investigated it could be useful calculate the coating thickness from the mass loss upon heating by TGA experiments as reported by Kuttner *et al.*.[38, 39]
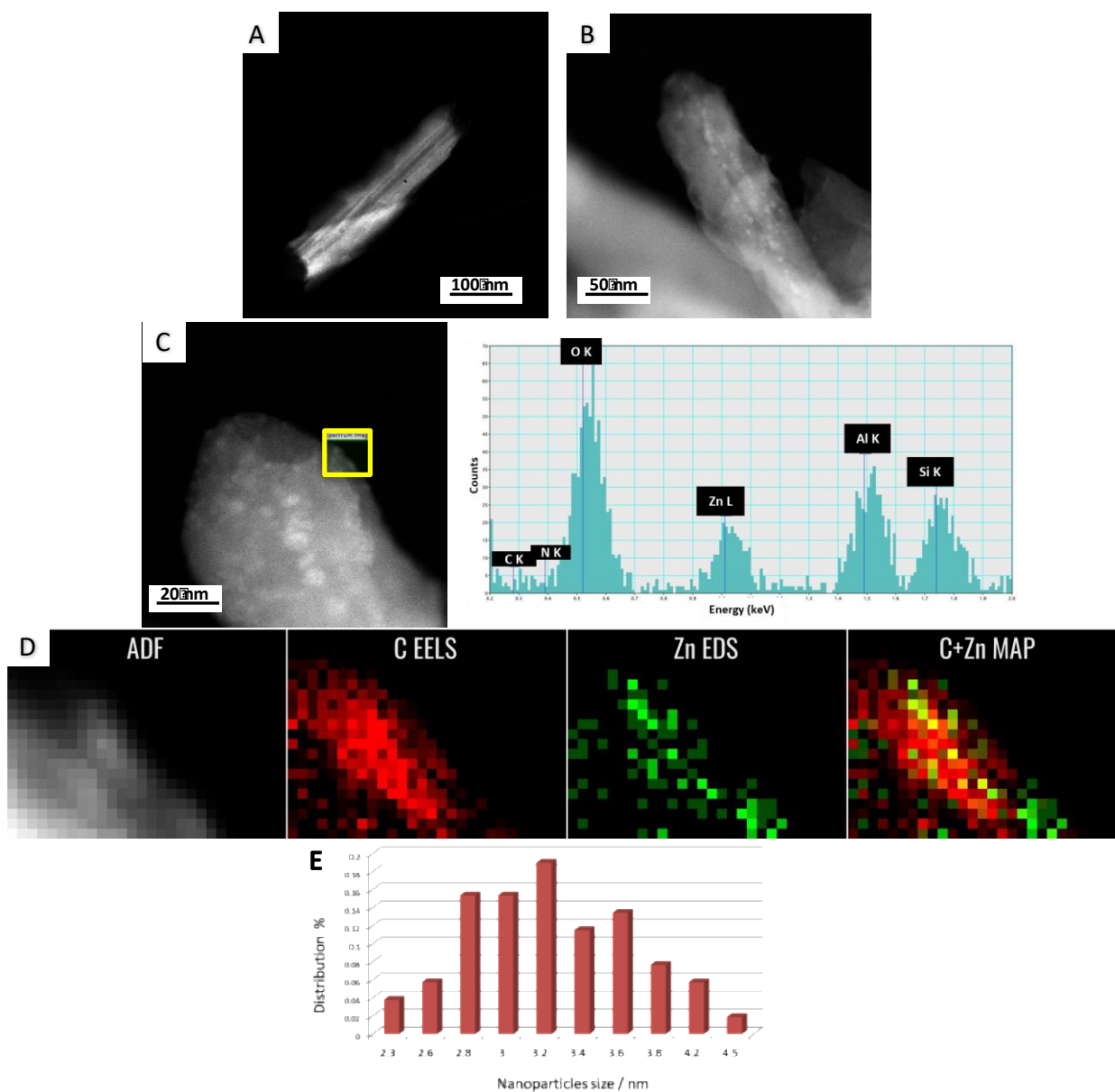
Figure 3. HAADF-STEM images of (a) pristine HNTs (b) HNTs@PDA, the insert indicates the EDX spectrum of the selected area; (c) scanning TEM-energy dispersive X-ray and EELS spectroscope elemental mapping results of HNTs@ZnO@PDA, (d) nanoparticles size distribution (n=55).

The TGA curves of the HNTs@PDA nanomaterial, obtained after 10 h and 24 h of reaction time, are shown in Figure 4, in comparison with that of the HNTs@ZnO precursor.

292 For all samples, the main weight loss occurs in the range 100-500 °C, then, at ~600 °C
293 stable mass values were registered. The HNTs@ZnO gradually lost water due to the
294 progressive dehydroxylation of structural Al−OH groups of HNTs[2] until the crystal
295 structure was completely modified at around 500 °C. A similar shape of TGA curve was
296 registered for both, HNTs@PDA nanomaterials, obtained after 10 h and 24 h of reaction
297 time, with degradation at lower temperature with respect to the HNTs@ZnO precursor.
298 Such finding agrees with the surface modification of the HNTs@ZnO by PDA which
299 decomposition easily occurred under air atmosphere in the range of temperature between
300 100-500 °C. Based on the overall weight loss of the HNTs@PDA, the estimated amount
301 of PDA deposited onto HNTs@ZnO was *ca.* 1.6 wt% that well corresponds to the
302 expected loading based on the concentration of dopamine hydrochloride solution used in
303 the preparation. No differences were found after 10 and 24 h of reaction, suggesting that
304 10 h are sufficient to deposit the maximum amount of PDA onto the HNTs and further
305 increasing the reaction time up to 24 h does not have any effect in agreement with DLS
306 data.

307   By assuming the site-selective/specific functionalization of HNTs surface which exploits the
308 basicity of ZnO nanoparticles anchored on it, inducing a "pin-point" polydopamine
309 polymerization and coating, the calculation of the coating thickness t relies on the ZnO
310 radius r, the densities ρ_i and the weight fractions w_i (of HNTs@PDA or HNTs@ZnO)
311 given by the mass loss as stated in the equation below:

312
$$t = \left(\sqrt{1 + \frac{w_{HNTs@PDA}}{w_{HNTs@ZnO}} \cdot \frac{\rho_{ZnO}}{\rho_{PDA}}} - 1 \right) r \qquad \text{(Eq. 1)}$$

313

314   This estimation relies on the assumption that all PDA coating was removed in the
315 heating process. The error of this estimation can be derived from Gaussian error
316 propagation as reported elsewhere.[38] We assumed an error of 0.25 nm for the radius,
317 0.1 g cm^{-3} for density and 0.1% for the mass loss. Density values were given by literature
318 (PDA 1.52 g cm^{-3})[40] and manufacturer (ZnO 5.61 g cm^{-3}). The calculated thickness of
319 polymer layers (1.50 ± 0.5 nm) is in good agreement with TEM estimation.

320   The FT-IR spectrum of HNTs@PDA showed, besides the characteristic bands of
321 HNTs,[26] additional bands (Figure 4b) in the range 3500−3100 cm^{-1} attributable to the

322 stretching of −N−H and −O−H groups, a peak at *ca.* 3100 cm^{-1} related to the stretching of

323 −C−H of aromatic rings, and a sharp peak at *ca.* 1680 cm^{-1} attributed to the −C=C−

324 stretching vibration.[41] In addition, in the ATR-IR spectrum, bands in the range 580-620

325 cm^{-1} were observed which could be due to the vibration of the aromatic skeleton of PDA

326 such as aromatic −C−H out-of-plane bend or the out-of-plane bend of −O−H groups of

327 catechol moieties (Figure S4).
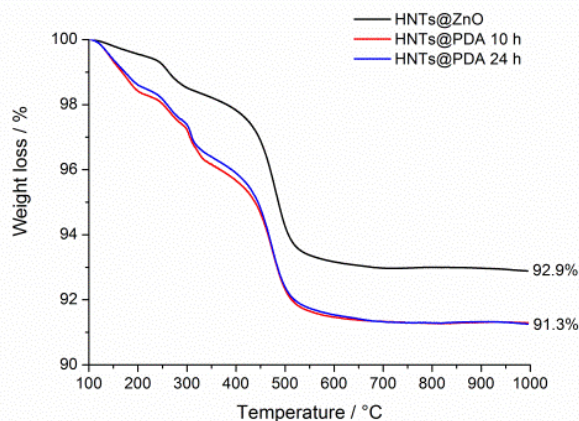
328
(a)
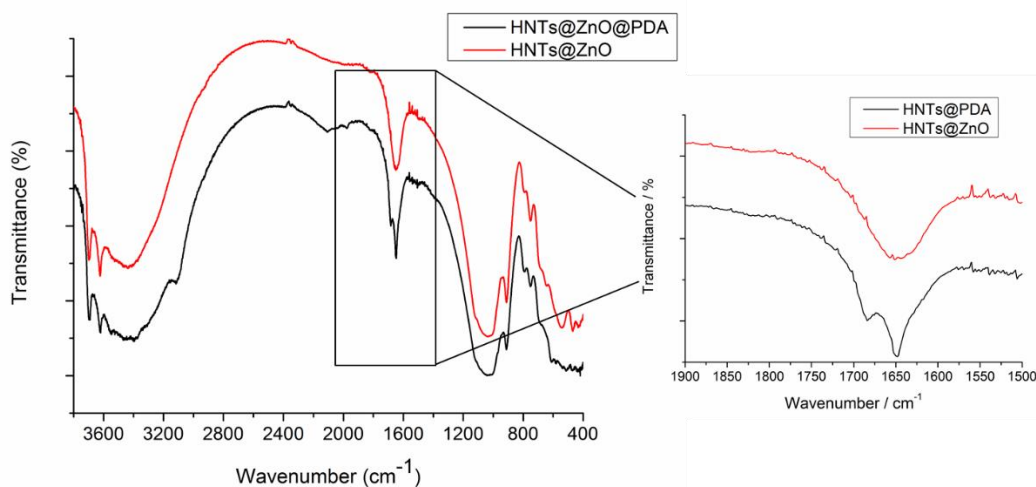
329
(b)

330 **Figure 4.** (a) Thermogravimetric curves of HNTs@ZnO and HNTs@PDA obtained after 10 h or 24 h of
331 treatment *vs* temperature registered under air flow; (b) FT-IR spectra of HNTs@ZnO and HNTs@PDA
332 nanomaterials.

333 EPR spectroscopy indicated for HNTs@PDA a single, ill-resolved and slightly

334 asymmetrical signal, consistent with the coexistence of O-centered semiquinone radicals

335 and related carbon-centered radicals on the PDA-coated nanostructures.[42-44] The

336 signal lineshape was found to be midway between gaussian and lorentzian. A similar

13

337 signal was observed on PDA-coated ZnO (ZnO@PDA) as a control, whereas HNTs and

338 HNTs@ZnO were EPR silent (Figure 5a).

339 Table 2 indicated nearly identical g-values and signal amplitudes (ΔB) for the

340 HNTs@PDA and ZnO@PDA samples, supporting a common origin of the signals.

341 However, a higher spin density was observed in the case of HNTs@PDA, suggesting an

342 intriguing effect of the halloysite support on the ZnO@PDA radical content. The power

343 saturation curves (Figure 5b) showed a plateau at high microwave power, indicating a

344 high degree of inhomogeneity in both the molecular nature and spatial distribution of the

345 paramagnetic centers. Noteworthy, despite an apparent similarity with the typical EPR

346 spectra of PDA reported in the literature,[43-45] the g-value measured in the case of

347 HNTs@PDA was slightly lower, suggesting that the balance of the O-centered versus

348 carbon-centered radicals was tipped toward the latter, with a more inhomogeneous

349 saturation profile. These differences will be the subject of separate investigation, as they

350 can yield interesting insights into the effect of the different polymerization conditions and

351 sample hydration.

352 **(a)**   **(b)**
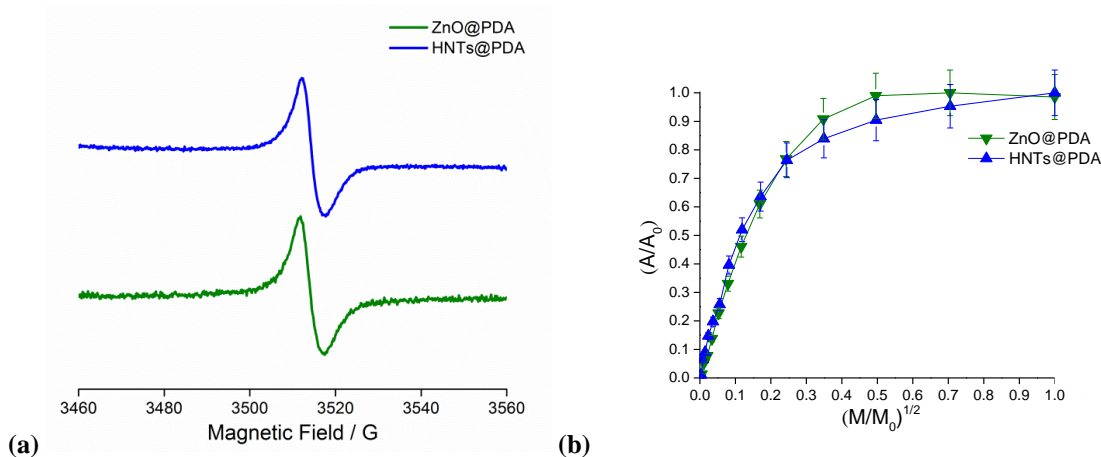
353 **Figure 5.** (a) EPR spectra and (b) Power saturation profiles (amplitude *vs.* power intensity) of ZnO@PDA

354 and HNTs@PDA samples.

355 **Table 2.** EPR parameters of the investigated samples. Experimental uncertainties are $\pm$ 0.0003 on g-factor,

356 $\pm$ 0.2 G on ΔB, $\pm$ 5% on line shape analysis, $\pm$ 10% on spin-density values.

	g-factor	ΔB /G	Gaussian lineshape Fraction	Spin density $\times 10^{-16}$ /spin g^{-1}
ZnO@PDA	2.0031	5.8	0.44	0.65
HNTs@PDA	2.0035	5.0	0.43	2.5

357

358   The optical properties of the HNTs@PDA nanomaterial were investigated by UV–*vis*
359   diffuse reflectance spectra (DRS) (Figure 6) in which the absorbance spectra were
360   obtained by applying the Kubelka–Munk function, $F(R_\infty)$.[46] The UV-*vis* spectrum of
361   HNTs@PDA proved likewise different from that of the HNTs@ZnO precursor. As shown
362   in Figure 6 and S5, HNTs@PDA exhibited broad absorption ranging from ultraviolet at
363   *ca.* 400 nm, attributed to the oxidation of dopamine into dopachrome and dopaindole, to
364   visible and NIR wavelengths following dopamine self-polymerization process,[47-49].
365   The untreated inorganic precursor exhibited instead a sharp absorption maximum of at *ca.*
366   370 nm due to the main electronic transition of ZnO nanoparticles.[28] Of course this
367   absorption could derived

368
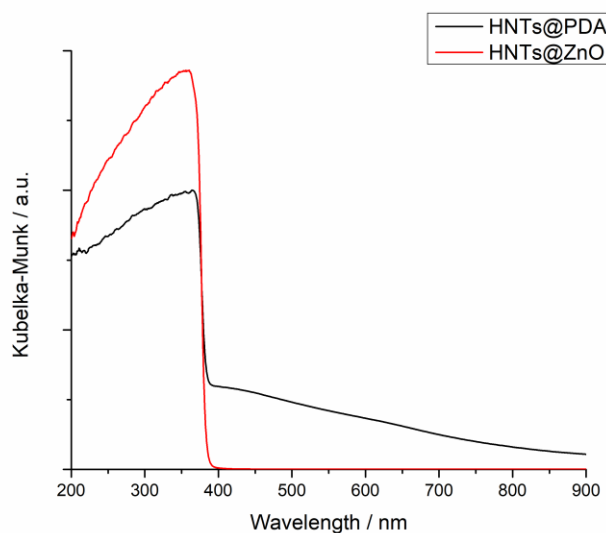
369

370   **Figure 6.** Absorbance spectra by applying the Kubelka e Munk function to DRS of HNTs@ZnO and
371   HNTs@PDA nanomaterials.

372   Turbidimetric analyses (Figure 7) showed that PDA coating affected the aqueous stability
373   of HNTs@PDA compared to both HNTs@ZnO and HNTs. It was concluded that the
374   PDA coating partly counteracted the destabilizing effect of ZnO nanoparticles on HNTs
375   suspensions which occurs after 700 min.
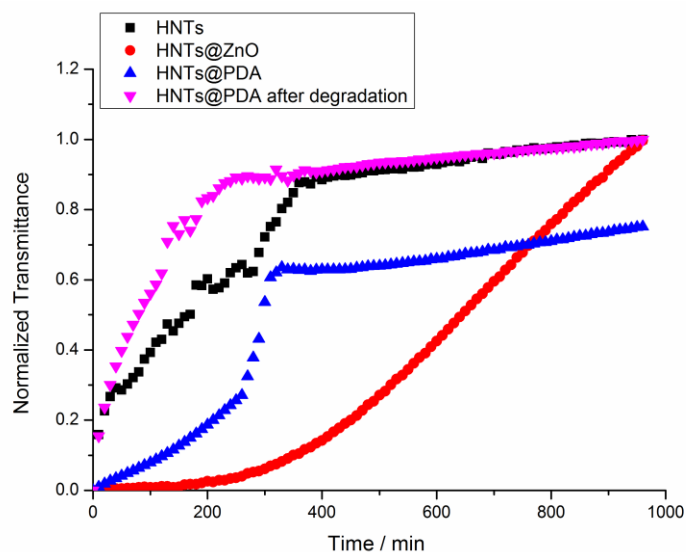
Figure 7. Normalized transmittance as a function of time for HNTs, HNTs@ZnO, HNTs@PDA and HNTs@PDA after degradation dispersions in water. The nanomaterial concentration is 1 mg mL^{-1} in all cases.

In further experiments, the PDA component in HNTs@PDA was investigated by a chemical degradation procedure commonly used for the characterization and quantitation of melanins in biological systems.[50] The method is based on degradation of the sample with alkaline hydrogen peroxide followed by HPLC determination of two typical degradation markers of indolic units, namely pyrrole-2,3-dicarboxylic acid (PDCA) and pyrrole-2,3,5-tricarboxylic acid (PTCA) (Figure S6).[31, 51, 52] Whereas PTCA may originate from both inner and terminal 2-linked units of 5,6-dihydroxyindole (DHI) derived from the oxidative cyclization of dopamine, PDCA can be taken as a specific marker of terminal DHI-indole units unsubstituted at the 2-position. Comparative analysis of PTCA and PDCA yields from HNTs@PDA and from reference PDA samples prepared by air oxidation of 1 mM and 10 mM dopamine in carbonate buffer at pH 8.5, suggested for the hybrid material a prevalence of dopamine dimerization, rather than intramolecular cyclization pathways (Table S1). After chemical degradation of the PDA component, the resulting dispersion showed the similar aqueous behavior of HNTs (Figure 6), suggesting removal of both PDA and ZnO by the alkaline hydrogen peroxide treatment.

3.1 Hyperthermia studies

16

Compared with other widely used photothermal agents, such as carbon-based nanomaterials, Cu-based semiconductor nanoparticles, organic polymers,[53] and metals nanoparticles (*e.g.* Au, Ag, and Pd),[54] PDA exhibit better biocompatibility due to its excellent biodegradability. Moreover, it possesses an excellent photothermal conversion efficiency of ~40%, which is much higher than that of other photothermal therapy species. PDA can effectively absorb and transfer NIR optical energy into heat at low laser power density and short irradiation time without damaging healthy tissues, enabling it to be a desirable photothermal therapeutic agent for tumor treatment and bacteria killing.[52, 55] Indeed, photothermal ability of a PDA based system could be crucial for regulating the drug release kinetics and coordinating the therapeutic activity of individual components.[16] To this aim, we investigated the NIR induced heat generation efficiency of the HNTs@PDA nanomaterial (10 mg mL^{-1} which correspond to PDA amount of 160 µg mL^{-1}) after irradiation in aqueous dispersion with an 810 nm diode laser beam. As illustrated in Figure 8a, the aqueous dispersion of the material induced a local thermic rise, generating a hyperthermia effect as a function of the irradiation time at an energy density of 0.5 W cm^{-3}. By increasing the laser power to 0.7 W cm^{-3} we observed an increase in the recorded temperature values reaching up to 50 °C. Conversely, the temperature of the aqueous dispersion of pristine HNTs and HNTs@ZnO, chosen as controls, exhibited only negligible change under NIR irradiation.

In further experiments, the photothermal conversion efficiency (η) of HNTs@PDA was determined. The η value was calculated by following a procedure reported elsewhere [49]:

$$\eta = \frac{hA\Delta T_{max} - Q_S}{I(1 - 10^{-A_\lambda})} \qquad \text{(Eq. 2)}$$

where h is the heat transfer coefficient, A is the surface area of the container, ΔT_{max} is the temperature change of the HNTs@PDA dispersion at the maximum steady-state temperature, I is the laser power, A_λ is the absorbance of the HNTs@PDA dispersion at 810 nm, Q_s is the heat associated with the light absorbance of the solvent. Q_s was calculated from $Q_S = hA\Delta T_{solvent}$, where $\Delta T_{solvent}$ is the maximum temperature change of water irradiated by the same light source at the same power intensity. The parameter set hA was determined by fitting temperature *vs.* time data to the equation (Figure 7b):

426
$$t = -\frac{\sum_i m_i C_{pi}}{hA} \ln(\theta) \qquad \text{(Eq. 3)}$$

427 where, m_i is the mass of component i, C_{pi} is the specific heat capacity of component i, t is

428 time, and θ is defined as the ratio of ΔT to ΔT_{max}). The summation $\sum_i m_i C_{pi}$ was

429 approximated by the mass and specific heat capacity of the solvent (water: 4.2 J g^{-1} $°C^{-1}$).

430 According to Equation 2, the η value of HNTs@PDA was determined to be 55%,

431 comparable to the reported values of the other eumelanin base system envisaged for this

432 purpose [13, 49, 56, 57].

433 **(a)**   **(b)**

434   **(c)**
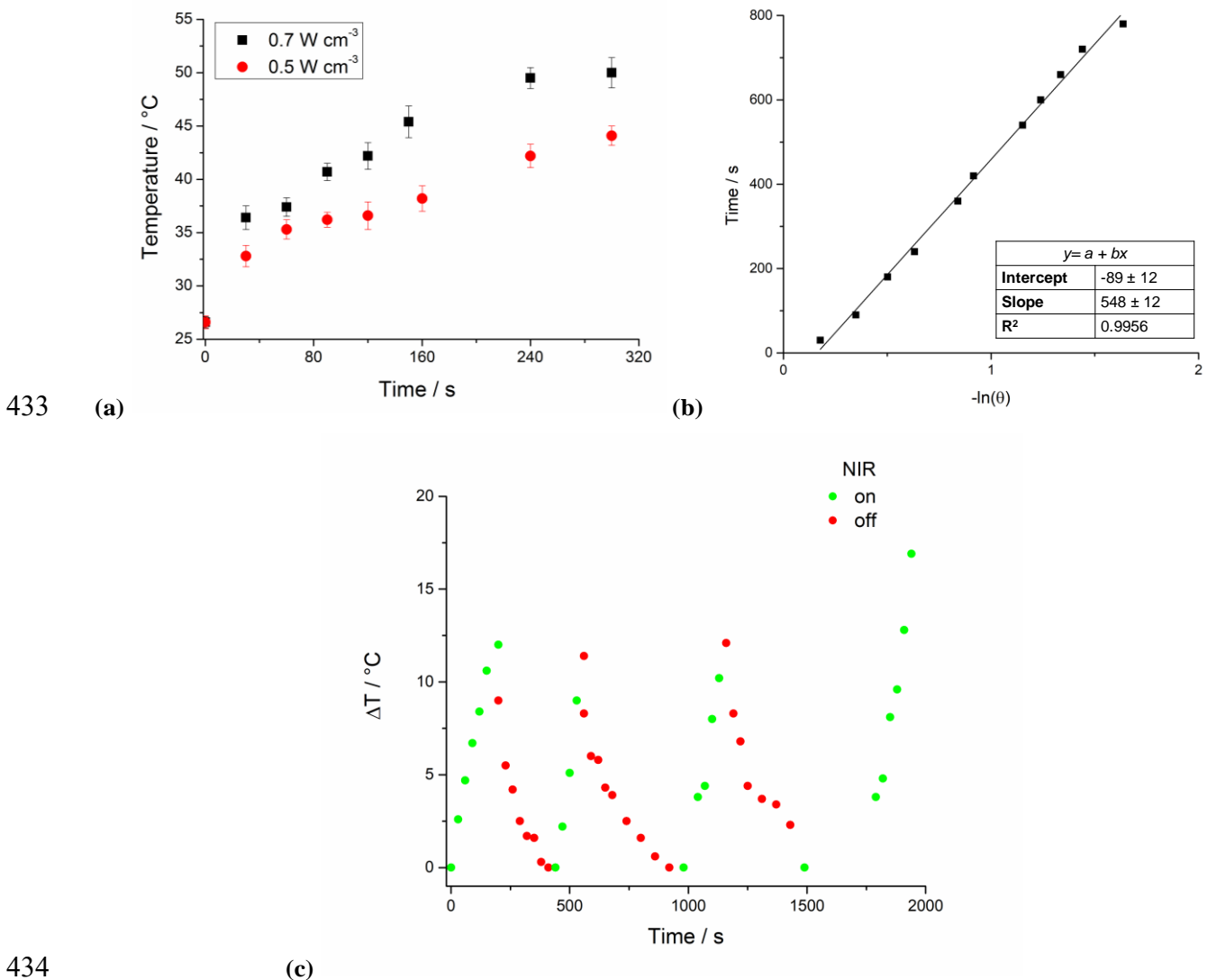
435 **Figure 8.** (a) Temperature change over time of aqueous dispersion of HNTs@PDA (10 mg mL^{-1} which

436 correspond to PDA amount of 160 μg mL^{-1}) upon irradiation by an 810 nm source at different energy

437 density. Reported are the mean ± SD values of three independent experiments run in triplicate. (b) Time *vs* -

18

438   ; (c) cyclic photothermal behavior of HNTs@PDA dispersion (10 mg mL^{-1}

439   which correspond to PDA amount in the nanomaterial of 160 μg mL^{-1}), sample irradiated for 300 s by an

440   810 nm sources at 0.7 W cm^{-3} followed by no irradiation until dispersion cooled to ambient temperature (*ca.*

441   600 s).

442

443   Finally, in order to assess the photothermal stability, four cycles of laser on/off operation

444   were performed (laser irradiation for 300 s and then cooling for 600 s) on the water

445   dispersion of HNTs@PDA (10 mg mL^{-1}) at an energy density of 0.7 W cm^{-3} with 810 nm

446   wavelength light. As shown in Figure 6c, no temperature change was detected during this

447   period, demonstrating the good photothermal stability of the prepared HNTs@PDA

448   nanomaterial.

449   **3.2. Secondary functionalization of HNTs@PDA**

450   The pin-point strategy adopted in our study could also provide a useful tool to achieve

451   site-specific functionalization of the outer surface of HNTs aimed *e.g.* at more effective

452   drug delivery systems. Accordingly, in preliminary experiments HNTs @PDA was

453   functionalized with biotin 2'-aminoethylamide [29] (**1**) in refluxing EtOH for 18 h

454   (Scheme 2).

455   Covalent linking of **1** to HNTs@PDA *via* imine bond formation was confirmed by FT-IR

456   spectroscopy (Figure 9a) showing the typical vibration bands of biotin [58] at *ca.* 2930,

457   2845, 1414 and 1260 cm^{-1} along with signals at *ca.* 1590 and 1470 cm^{-1} which could be

458   attributed to the stretching bands of a Schiff base.
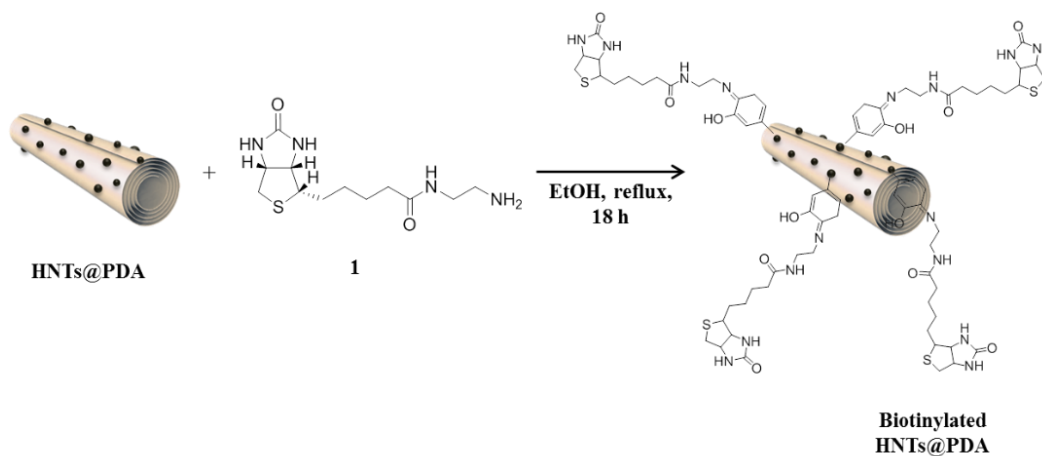
459

460   **Scheme 2.** Schematic representation of the synthesis of biotinylated HNTs@PDA nanomaterial.

461

462   Biotinylated HNTs@PDA was finally investigated for its receptor-binding capacity

463   toward the 4-hydroxyazobenzene-2-carboxylic acid (HABA)/Avidin complex by means

464   of UV-*vis* spectroscopy. As shown in Figure 9b, a decrease in the absorption maximum

465   band of HABA/Avidin complex was observed following addition of biotinylated

466   HNTs@PDA, consistent with displacement of HABA molecules from the avidin

467   complex. This assay allowed to estimate the amount of biotin grafted on HNTs@PDA in

468   the order of 5 wt%, corresponding to a degree of functionalization of the PDA layer of *ca.*

469   0.21 mmol g^{-1}) (see SI for details).

470   **(a)**

(b)
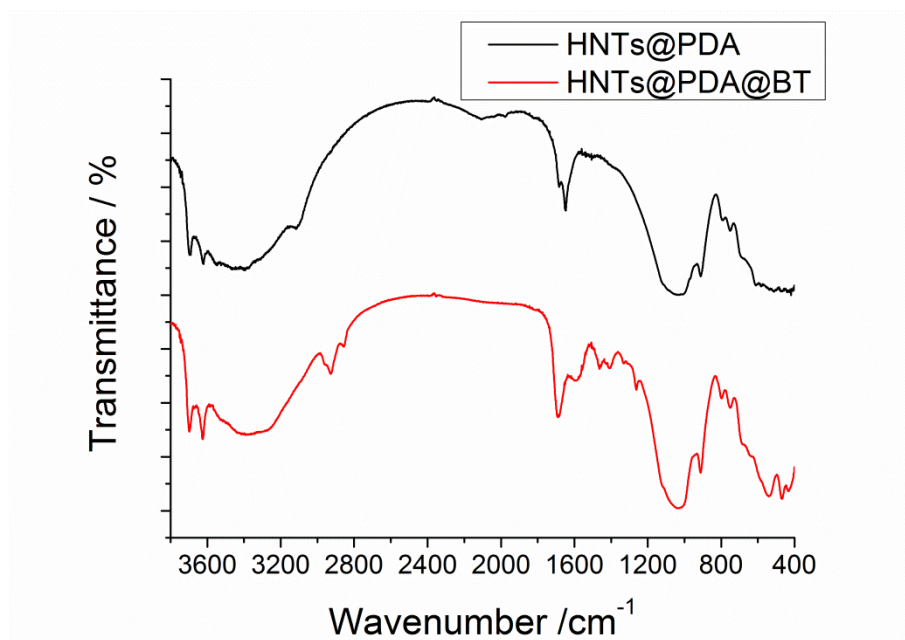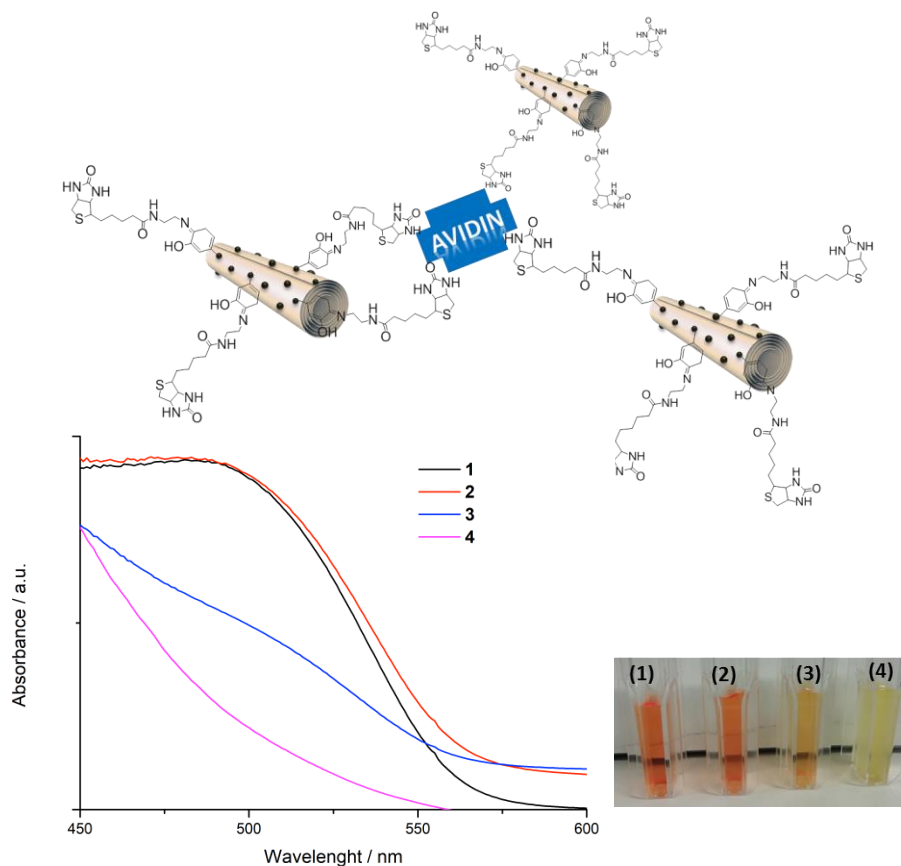
Figure 9. (a) FT-IR spectra of HNTs@PDA nanomaterial before and after biotinylation; (b) UV-*vis* spectra of: (1) HABA/Avidin complex (black line), (2) HABA/Avidin complex in the presence of HNTs@PDA (red line), (3) HABA/Avidin complex in the presence of biotinylated HNTs@PDA (0.6 mg mL^{-1}) (blue line), (4) HABA/Avidin complex in the presence of biotinylated HNTs@PDA (6 mg mL^{-1}) (purple line).

DLS analysis after biotinylation and interaction with avidin indicated a decrease in the Z-average size and polydispersity index of the HNTs@PDA (940 ± 110 nm and 0.44 for biotinylated HNTs@PDA; 970 ± 110 nm and 0.28 after interaction with avidin, respectively) because of the introduction of hydrophilic groups reducing aggregation in aqueous media. ζ-potential measurements revealed an almost neutral surface both after the biotinylation reaction and avidin interaction (0 ± 2 mV, in both cases), corroborating the secondary modification.

HAADF-STEM images of biotinylated HNTs@PDA (Figure 10a-b) showed that the morphology of the tubes was unaffected by the biotinylation reaction. The nanomaterial exhibited the characteristic hollow tubular structure of halloysite with some aggregates (Figure 10a) which could be due to the interactions between the grafted organic units. The

21

488 EDS spectrum obtained by integration over the entire region confirmed the presence of
489 organic C along with the Zn, Al, Si and O atoms related to the inorganic support.

490

(a)

491 **(b)**
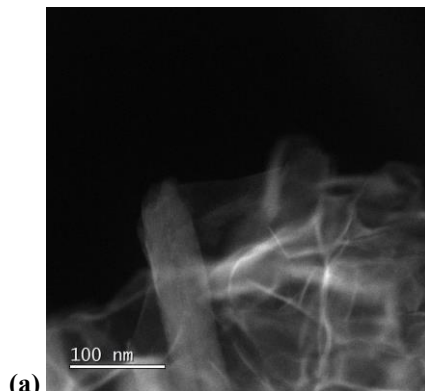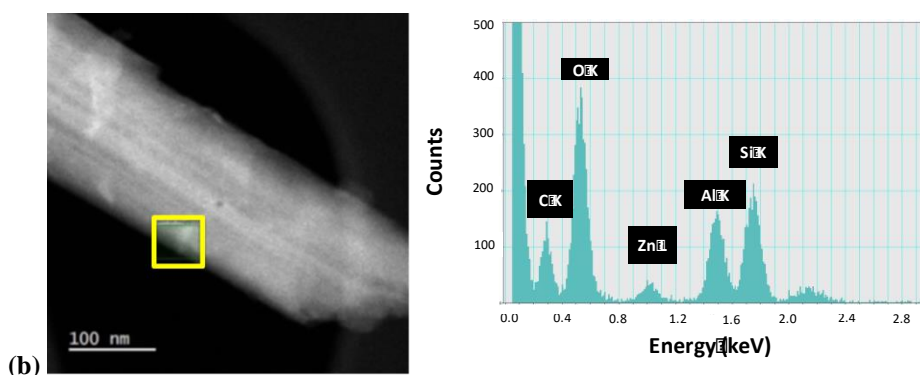
492 **Figure 10.** (a-b) HAADF-STEM images of HNTs@PDA, the insert indicates the EDX spectrum of the
493 selected area.

494 **CONCLUSIONS**

495 HNTs represent a versatile core structure for the design of functional nanosystems of biomedical
496 interest. However, the development of selective methodologies for the site-controlled
497 functionalization of the nanotubes at specific sites is not an easy task. This study disclosed an
498 effective strategy for the clean and selective, site-specific, "pin-point" functionalization of the
499 outer surface of halloysite nanotubes by PDA. The site-specific deposition of dopamine to
500 produce PDA nanocoating was achieved with high precision by exposing HNTs@ZnO, endowed
501 with basic site through the anchoring of ZnO nanoparticles, to a dopamine solution at neutral pH
502 under conditions in which no PDA precipitation was observed. The rapid surface-induced solid-
503 state polymerization process ensured both the desired confinement of the coating to the basic
504 nanosurfaces and thickness control to *ca.* 1 nm without contamination of the hybrid architecture
505 by PDA particles precipitating in the medium. Up to now, relevant publications on HNTs
506 reported the PDA coating on the overall HNTs external surface under basic conditions without

22

polymeration control.[20, 59] Furthermore, the proposed strategy is different from the classical PDA dip-coating technology because it introduces a rationale for: 1) high site-selective functionalization; 2) no need for an alkaline medium, which is an advantage regarding material stability or processing issues, 3) a clean protocol, avoiding waste of material by uncontrolled precipitation, as with the dip-coating protocol, which may often contaminate delicate or high value-added systems.[60, 61]

The PDA coating of halloysite allowed to introduce additional properties to HNTs such as the possibility to achieve a local thermic rise under NIR irradiation which could be crucial to selectively kill cancer cells. In light of the NIR absorption capacity and good photothermal conversion efficiency of HNTs@PDA as well as the easy of PDA surface decoration with other functional molecules, for the existence of functional groups of catechol and amine, as herein demonstrated with the secondary modification of HNTs@PDA nanomaterial, this work open the doorway to novel strategies for selective nanofunctionalization and nanopatterning of halloysite for development of multifunctional delivery systems thus expanding the current toolbox of mussel-inspired coating technologies. Future work will be devoted to assessing the feasibility of the nanomaterial obtained as carrier system for biologically active molecules and/or fluorescent molecules for further developments in theranostics and bioimaging for cancer treatment.

Supporting Information. Calculation of biotin loading, diffusion coefficient of HNTs coating by PDA as a function of time, SEM images of pristine HNTs and HNTs@ZnO, and STEM image of HNTs@ZnO. ATR and UV-*vis* spectra of HNTs@ZnO and HNTs@PDA nanomaterials, PTCA and PDCA structures, yields of PTCA and PDCA produced by oxidative degradation of HNTs@PDA and polydopamine.

REFERENCES

[1] N. Mauro, M.A. Utzeri, S.E. Drago, G. Buscarino, G. Cavallaro, G. Giammona, Carbon nanodots as functional excipient to develop highly stable and smart PLGA nanoparticles useful in cancer theranostics, Pharmaceutics 12(11) (2020) 1-15.

[2] M. Massaro, R. Noto, S. Riela, Past, Present and Future Perspectives on Halloysite Clay Minerals, Molecules 25(20) (2020) 4863.

[3] M. Tharmavaram, G. Pandey, D. Rawtani, Surface modified halloysite nanotubes: A flexible interface for biological, environmental and catalytic applications, Advances in Colloid and Interface Science 261 (2018) 82-101.

[4] A. Glotov, A. Stavitskaya, Y. Chudakov, E. Ivanov, W. Huang, V. Vinokurov, A. Zolotukhina, A. Maximov, E. Karakhanov, Y. Lvov, Mesoporous Metal Catalysts Templated on Clay Nanotubes, Bulletin of the Chemical Society of Japan 92(1) (2019) 61-69.

[5] A.V. Stavitskaya, E.A. Kozlova, A.Y. Kurenkova, A.P. Glotov, D.S. Selischev, E.V. Ivanov, D.V. Kozlov, V.A. Vinokurov, R.F. Fakhrullin, Y.M. Lvov, Ru/CdS Quantum Dots Templated on Clay Nanotubes as Visible-Light-Active Photocatalysts: Optimization of S/Cd Ratio and Ru Content, Chemistry – A European Journal 26(57) (2020) 13085-13092.

[6] Y. Lvov, A. Panchal, Y. Fu, R. Fakhrullin, M. Kryuchkova, S. Batasheva, A. Stavitskaya, A. Glotov, V. Vinokurov, Interfacial Self-Assembly in Halloysite Nanotube Composites, Langmuir 35(26) (2019) 8646-8657.

[7] A.V. Stavitskaya, A.A. Novikov, M.S. Kotelev, D.S. Kopitsyn, E.V. Rozhina, I.R. Ishmukhametov, R.F. Fakhrullin, E.V. Ivanov, Y.M. Lvov, V.A. Vinokurov, Fluorescence and Cytotoxicity of Cadmium Sulfide Quantum Dots Stabilized on Clay Nanotubes, Nanomaterials 8(6) (2018) 391.

[8] M. Massaro, S. Riela, G. Cavallaro, C.G. Colletti, S. Milioto, R. Noto, G. Lazzara, Ecocompatible Halloysite/Cucurbit[8]uril Hybrid as Efficient Nanosponge for Pollutants Removal, ChemistrySelect 1(8) (2016) 1773-1779.

[9] A. Gładysz-Płaska, M. Majdan, B. Tarasiuk, D. Sternik, E. Grabias, The use of halloysite functionalized with isothiouronium salts as an organic/inorganic hybrid adsorbent for uranium(VI) ions removal, Journal of Hazardous Materials 354 (2018) 133-144.

[10] M. Massaro, G. Barone, G. Biddeci, G. Cavallaro, F. Di Blasi, G. Lazzara, G. Nicotra, C. Spinella, G. Spinelli, S. Riela, Halloysite nanotubes-carbon dots hybrids multifunctional nanocarrier with positive cell target ability as a potential non-viral vector for oral gene therapy, Journal of Colloid and Interface Science 552 (2019) 236-246.

[11] H. Zhang, T. Ren, Y. Ji, L. Han, Y. Wu, H. Song, L. Bai, X. Ba, Selective Modification of Halloysite Nanotubes with 1-Pyrenylboronic Acid: A Novel Fluorescence Probe with Highly Selective and Sensitive Response to Hyperoxide, ACS Applied Materials and Interfaces 7(42) (2015) 23805-23811.

579 [12] W.O. Yah, A. Takahara, Y.M. Lvov, Selective modification of halloysite lumen with
580 octadecylphosphonic acid: New inorganic tubular micelle, Journal of the American Chemical
581 Society 134(3) (2012) 1853-1859.
582 [13] C. Xue, M. Li, C. Liu, Y. Li, Y. Fei, Y. Hu, K. Cai, Y. Zhao, Z. Luo, NIR-Actuated Remote
583 Activation of Ferroptosis in Target Tumor Cells through a Photothermally Responsive Iron-
584 Chelated Biopolymer Nanoplatform, Angewandte Chemie International Edition 60(16) (2021)
585 8938-8947.
586 [14] Y. Yang, J. Liu, X. Sun, L. Feng, W. Zhu, Z. Liu, M. Chen, Near-infrared light-activated
587 cancer cell targeting and drug delivery with aptamer-modified nanostructures, Nano Research
588 9(1) (2016) 139-148.
589 [15] H. Cao, Y. Yang, M. Liang, Y. Ma, N. Sun, X. Gao, J. Li, Pt@polydopamine nanoparticles
590 as nanozymes for enhanced photodynamic and photothermal therapy, Chemical Communications
591 57(2) (2021) 255-258.
592 [16] M. Li, X. Sun, N. Zhang, W. Wang, Y. Yang, H. Jia, W. Liu, NIR-Activated Polydopamine-
593 Coated Carrier-Free "Nanobomb" for In Situ On-Demand Drug Release, Advanced Science 5(7)
594 (2018) 1800155.
595 [17] J. Feng, H. Fan, D.A. Zha, L. Wang, Z. Jin, Characterizations of the formation of
596 polydopamine-coated halloysite nanotubes in various pH environments, Langmuir 32(40) (2016)
597 10377-10386.
598 [18] F. Ponzio, J. Barthès, J. Bour, M. Michel, P. Bertani, J. Hemmerlé, M. d'Ischia, V. Ball,
599 Oxidant Control of Polydopamine Surface Chemistry in Acids: A Mechanism-Based Entry to
600 Superhydrophilic-Superoleophobic Coatings, Chemistry of Materials 28(13) (2016) 4697-4705.
601 [19] G. Zeng, Z. Ye, Y. He, X. Yang, J. Ma, H. Shi, Z. Feng, Application of dopamine-modified
602 halloysite nanotubes/PVDF blend membranes for direct dyes removal from wastewater,
603 Chemical Engineering Journal 323 (2017) 572-583.
604 [20] S. Sadjadi, G. Lazzara, M. Malmir, M.M. Heravi, Pd nanoparticles immobilized on the
605 poly-dopamine decorated halloysite nanotubes hybridized with N-doped porous carbon
606 monolayer: A versatile catalyst for promoting Pd catalyzed reactions, Journal of Catalysis 366
607 (2018) 245-257.
608 [21] Y. Liu, W. Tu, M. Chen, L. Ma, B. Yang, Q. Liang, Y. Chen, A mussel-induced method to
609 fabricate reduced graphene oxide/halloysite nanotubes membranes for multifunctional
610 applications in water purification and oil/water separation, Chemical Engineering Journal 336
611 (2018) 263-277.
612 [22] H. Kang, X. Liu, S. Zhang, J. Li, Functionalization of halloysite nanotubes (HNTs) via
613 mussel-inspired surface modification and silane grafting for HNTs/soy protein isolate
614 nanocomposite film preparation, RSC Advances 7(39) (2017) 24140-24148.
615 [23] S. Ganguly, N.C. Das, Synthesis of Mussel Inspired Polydopamine Coated Halloysite
616 Nanotubes Based Semi-IPN: An Approach to Fine Tuning in Drug Release and Mechanical
617 Toughening, Macromolecular Symposia 382(1) (2018) 1800076.
618 [24] W.O. Yah, H. Xu, H. Soejima, W. Ma, Y. Lvov, A. Takahara, Biomimetic dopamine
619 derivative for selective polymer modification of halloysite nanotube lumen, Journal of the
620 American Chemical Society 134(29) (2012) 12134-12137.
621 [25] R.S. Hebbar, A.M. Isloor, K. Ananda, A.F. Ismail, Fabrication of polydopamine
622 functionalized halloysite nanotube/polyetherimide membranes for heavy metal removal, Journal
623 of Materials Chemistry A 4(3) (2016) 764-774.

624 [26] M. Massaro, F. Armetta, G. Cavallaro, D.F. Chillura Martino, M. Gruttadauria, G. Lazzara,
625 S. Riela, M. d'Ischia, Effect of halloysite nanotubes filler on polydopamine properties, Journal of
626 Colloid and Interface Science 555 (2019) 394-402.
627 [27] F. Wu, J. Zheng, Z. Li, M. Liu, Halloysite nanotubes coated 3D printed PLA pattern for
628 guiding human mesenchymal stem cells (hMSCs) orientation, Chemical Engineering Journal 359
629 (2019) 672-683.
630 [28] M. Massaro, M. Casiello, L. D'Accolti, G. Lazzara, A. Nacci, G. Nicotra, R. Noto, A.
631 Pettignano, C. Spinella, S. Riela, One-pot synthesis of ZnO nanoparticles supported on halloysite
632 nanotubes for catalytic applications, Applied Clay Science 189 (2020).
633 [29] P. Bottari, R. Aebersold, F. Turecek, M.H. Gelb, Design and Synthesis of Visible Isotope-
634 Coded Affinity Tags for the Absolute Quantification of Specific Proteins in Complex Mixtures,
635 Bioconjugate Chemistry 15(2) (2004) 380-388.
636 [30] F. Sannino, P. Pernice, C. Imparato, A. Aronne, G. D'Errico, L. Minieri, M. Perfetti, D.
637 Pirozzi, Hybrid TiO2–acetylacetonate amorphous gel-derived material with stably adsorbed
638 superoxide radical active in oxidative degradation of organic pollutants, RSC Advances 5(114)
639 (2015) 93831-93839.
640 [31] N.F. Della Vecchia, R. Avolio, M. Alfè, M.E. Errico, A. Napolitano, M. d'Ischia, Building-
641 Block Diversity in Polydopamine Underpins a Multifunctional Eumelanin-Type Platform
642 Tunable Through a Quinone Control Point, Advanced Functional Materials 23(10) (2013) 1331-
643 1340.
644 [32] N. Mauro, C. Scialabba, G. Cavallaro, M. Licciardi, G. Giammona, Biotin-Containing
645 Reduced Graphene Oxide-Based Nanosystem as a Multieffect Anticancer Agent: Combining
646 Hyperthermia with Targeted Chemotherapy, Biomacromolecules 16(9) (2015) 2766-2775.
647 [33] R. Puleio, M. Licciardi, P. Varvarà, C. Scialabba, G. Cassata, L. Cicero, G. Cavallaro, G.
648 Giammona, Effect of actively targeted copolymer coating on solid tumors eradication by gold
649 nanorods-induced hyperthermia, International Journal of Pharmaceutics 587 (2020) 119641.
650 [34] M. Michalik, J. Szymańczyk, M. Stajnke, T. Ochrymiuk, A. Cenian, Medical Applications
651 of Diode Lasers: Pulsed versus Continuous Wave (cw) Regime, Micromachines 12(6) (2021)
652 710.
653 [35] C. Kuttner, P.C. Maier, C. Kunert, H. Schlaad, A. Fery, Direct Thiol–Ene Photocoating of
654 Polyorganosiloxane Microparticles, Langmuir 29(52) (2013) 16119-16126.
655 [36] M. Arzillo, G. Mangiapia, A. Pezzella, R.K. Heenan, A. Radulescu, L. Paduano, M.
656 d'Ischia, Eumelanin Buildup on the Nanoscale: Aggregate Growth/Assembly and Visible
657 Absorption Development in Biomimetic 5,6-Dihydroxyindole Polymerization,
658 Biomacromolecules 13(8) (2012) 2379-2390.
659 [37] S. Hong, Y.S. Na, S. Choi, I.T. Song, W.Y. Kim, H. Lee, Non-Covalent Self-Assembly and
660 Covalent Polymerization Co-Contribute to Polydopamine Formation, Advanced Functional
661 Materials 22(22) (2012) 4711-4717.
662 [38] C. Kuttner, M. Tebbe, H. Schlaad, I. Burgert, A. Fery, Photochemical Synthesis of
663 Polymeric Fiber Coatings and Their Embedding in Matrix Material: Morphology and
664 Nanomechanical Properties at the Fiber–Matrix Interface, ACS Applied Materials & Interfaces
665 4(7) (2012) 3484-3492.
666 [39] C. Kuttner, A. Hanisch, H. Schmalz, M. Eder, H. Schlaad, I. Burgert, A. Fery, Influence of
667 the Polymeric Interphase Design on the Interfacial Properties of (Fiber-Reinforced) Composites,
668 ACS Applied Materials & Interfaces 5(7) (2013) 2469-2478.

669 [40] N. Nishizawa, A. Kawamura, M. Kohri, Y. Nakamura, S. Fujii, Polydopamine Particle as a
670 Particulate Emulsifier, Polymers 8(3) (2016) 62.
671 [41] R.A. Zangmeister, T.A. Morris, M.J. Tarlov, Characterization of Polydopamine Thin Films
672 Deposited at Short Times by Autoxidation of Dopamine, Langmuir 29(27) (2013) 8619-8628.
673 [42] K. Tadyszak, R. Mrówczyński, R. Carmieli, Electron Spin Relaxation Studies of
674 Polydopamine Radicals, The Journal of Physical Chemistry B 125(3) (2021) 841-849.
675 [43] R. Mrówczyński, L.E. Coy, B. Scheibe, T. Czechowski, M. Augustyniak-Jabłokow, S.
676 Jurga, K. Tadyszak, Electron Paramagnetic Resonance Imaging and Spectroscopy of
677 Polydopamine Radicals, The Journal of Physical Chemistry B 119(32) (2015) 10341-10347.
678 [44] N.F. Della Vecchia, A. Luchini, A. Napolitano, G. D'Errico, G. Vitiello, N. Szekely, M.
679 d'Ischia, L. Paduano, Tris Buffer Modulates Polydopamine Growth, Aggregation, and
680 Paramagnetic Properties, Langmuir 30(32) (2014) 9811-9818.
681 [45] P. Manini, P. Margari, C. Pomelli, P. Franchi, G. Gentile, A. Napolitano, L. Valgimigli, C.
682 Chiappe, V. Ball, M. d'Ischia, Nanoscale Disassembly and Free Radical Reorganization of
683 Polydopamine in Ionic Liquids, The Journal of Physical Chemistry B 120(46) (2016) 11942-
684 11950.
685 [46] E.I. García-López, F.R. Pomilla, E. Bloise, X.F. Lü, G. Mele, L. Palmisano, G. Marcì,
686 C3N4 Impregnated with Porphyrins as Heterogeneous Photocatalysts for the Selective Oxidation
687 of 5-Hydroxymethyl-2-Furfural Under Solar Irradiation, Topics in Catalysis (2020).
688 [47] J. Wang, G. Ma, W. Huang, Y. He, Visible-light initiated polymerization of dopamine in a
689 neutral environment for surface coating and visual protein detection, Polymer Chemistry 9(42)
690 (2018) 5242-5247.
691 [48] H. Xu, X. Liu, D. Wang, Interfacial Basicity-Guided Formation of Polydopamine Hollow
692 Capsules in Pristine O/W Emulsions – Toward Understanding of Emulsion Template Roles,
693 Chemistry of Materials 23(23) (2011) 5105-5110.
694 [49] Y. Liu, K. Ai, J. Liu, M. Deng, Y. He, L. Lu, Dopamine-Melanin Colloidal Nanospheres:
695 An Efficient Near-Infrared Photothermal Therapeutic Agent for In Vivo Cancer Therapy,
696 Advanced Materials 25(9) (2013) 1353-1359.
697 [50] A. Napolitano, A. Pezzella, M.R. Vincensi, G. Prota, Oxidative degradation of melanins to
698 pyrrole acids: A model study, Tetrahedron 51(20) (1995) 5913-5920.
699 [51] K. Wakamatsu, S. Ito, Advanced Chemical Methods in Melanin Determination, Pigment
700 Cell Research 15(3) (2002) 174-183.
701 [52] L. Panzella, P. Manini, G. Monfrecola, M. D'Ischia, A. Napolitano, An easy-to-run method
702 for routine analysis of eumelanin and pheomelanin in pigmented tissues, Pigment Cell Research
703 20(2) (2007) 128-133.
704 [53] X. Luo, J. Zhang, Y.-P. Wu, X. Yang, X.-P. Kuang, W.-X. Li, Y.-F. Li, R.-R. He, M. Liu,
705 Multifunctional HNT@Fe3O4@PPy@DOX Nanoplatform for Effective Chemo-Photothermal
706 Combination Therapy of Breast Cancer with MR Imaging, ACS Biomaterials Science &
707 Engineering 6(6) (2020) 3361-3374.
708 [54] Y. Zeng, D. Zhang, M. Wu, Y. Liu, X. Zhang, L. Li, Z. Li, X. Han, X. Wei, X. Liu, Lipid-
709 AuNPs@PDA Nanohybrid for MRI/CT Imaging and Photothermal Therapy of Hepatocellular
710 Carcinoma, ACS Applied Materials & Interfaces 6(16) (2014) 14266-14277.
711 [55] W. Chen, Y. Wang, M. Qin, X. Zhang, Z. Zhang, X. Sun, Z. Gu, Bacteria-Driven Hypoxia
712 Targeting for Combined Biotherapy and Photothermal Therapy, ACS Nano 12(6) (2018) 5995-
713 6005.

714 [56] Y. Sun, E.W. Davis, Facile fabrication of polydopamine nanotubes for combined chemo-
715 photothermal therapy, Journal of Materials Chemistry B 7(43) (2019) 6828-6839.
716 [57] X. Cao, H. Liu, X. Yang, J. Tian, B. Luo, M. Liu, Halloysite nanotubes@polydopamine
717 reinforced polyacrylamide-gelatin hydrogels with NIR light triggered shape memory and self-
718 healing capability, Composites Science and Technology 191 (2020) 108071.
719 [58] V. Balan, I.A. Petrache, M.I. Popa, M. Butnaru, E. Barbu, J. Tsibouklis, L. Verestiuc,
720 Biotinylated chitosan-based SPIONs with potential in blood-contacting applications, Journal of
721 Nanoparticle Research 14(2) (2012) 730.
722 [59] M. Karolina Pierchala, F.B. Kadumudi, M. Mehrali, T.-G. Zsurzsan, P.J. Kempen, M.P.
723 Serdeczny, J. Spangenberg, T.L. Andresen, A. Dolatshahi-Pirouz, Soft Electronic Materials with
724 Combinatorial Properties Generated via Mussel-Inspired Chemistry and Halloysite Nanotube
725 Reinforcement, ACS Nano 15(6) (2021) 9531-9549.
726 [60] V. Ball, D.D. Frari, V. Toniazzo, D. Ruch, Kinetics of polydopamine film deposition as a
727 function of pH and dopamine concentration: Insights in the polydopamine deposition
728 mechanism, Journal of Colloid and Interface Science 386(1) (2012) 366-372.
729 [61] F. Bernsmann, V. Ball, F. Addiego, A. Ponche, M. Michel, J.J.d.A. Gracio, V. Toniazzo, D.
730 Ruch, Dopamine−Melanin Film Deposition Depends on the Used Oxidant and Buffer Solution,
731 Langmuir 27(6) (2011) 2819-2825.

732